

# Imaging semiconductor-to-metal transition and topological flat bands of twisted bilayer MoTe<sub>2</sub>

Yufeng Liu<sup>1,2†</sup>, Yu Gu<sup>1†</sup>, Ting Bao<sup>3,4†</sup>, Ning Mao<sup>5</sup>, Can Li<sup>1</sup>, Shudan Jiang<sup>1</sup>, Liang Liu<sup>1,2,8</sup>, Dandan Guan<sup>1,2,8</sup>, Yaoyi Li<sup>1,2,8</sup>, Hao Zheng<sup>1,2,8</sup>, Canhua Liu<sup>1,2,8</sup>, Kenji Watanabe<sup>6</sup>, Takashi Taniguchi<sup>7</sup>, Wenhui Duan<sup>4</sup>, Jinfeng Jia<sup>1,2,8</sup>, Xiaoxue Liu<sup>1,2,8</sup>, Yang Zhang<sup>3,9\*</sup>, Tingxin Li<sup>1,2,8\*</sup>, and Shiyong Wang<sup>1,2,8\*</sup>

<sup>1</sup>Key Laboratory of Artificial Structures and Quantum Control (Ministry of Education), School of Physics and Astronomy, Shanghai Jiao Tong University, Shanghai 200240, China

<sup>2</sup>Tsung-Dao Lee Institute, Shanghai Jiao Tong University, Shanghai, 201210, China

<sup>3</sup>Department of Physics and Astronomy, University of Tennessee, Knoxville, TN 37996, USA

<sup>4</sup>Department of Physics, Tsinghua University, Beijing 100084, China

<sup>5</sup>Max Planck Institute for Chemical Physics of Solids, 01187, Dresden, Germany

<sup>6</sup>Research Center for Electronic and Optical Materials, National Institute for Materials Science, 1-1 Namiki, Tsukuba 305-0044, Japan

<sup>7</sup>Research Center for Materials Nanoarchitectonics, National Institute for Materials Science, 1-1 Namiki, Tsukuba 305-0044, Japan

<sup>8</sup>Hefei National Laboratory, Hefei 230088, China

<sup>9</sup>Min H. Kao Department of Electrical Engineering and Computer Science, University of Tennessee, Knoxville, Tennessee 37996, USA

<sup>†</sup>These authors contribute equally to this work.

\*Emails: [yangzhang@utk.edu](mailto:yangzhang@utk.edu), [txli89@sjtu.edu.cn](mailto:txli89@sjtu.edu.cn), [shiyong.wang@sjtu.edu.cn](mailto:shiyong.wang@sjtu.edu.cn)

## Abstract

**Two-dimensional (2D) moiré materials have emerged as a highly tunable platform for investigating novel quantum states of matter arising from strong electronic correlations and nontrivial band topology<sup>1-4</sup>. Recently, topological flat bands formed in 2D semiconducting moiré superlattices have attracted great interests<sup>5-32</sup>. In particular, a series of topological quantum phases, including the long-sought fractional quantum anomalous Hall (FQAH) effect, have recently been experimentally observed<sup>14-22</sup> in twisted bilayer MoTe<sub>2</sub> (tMoTe<sub>2</sub>). However, the microscopic information of tMoTe<sub>2</sub> moiré superlattice and its electronic structure**

is still lacking. Here, we present scanning tunneling microscopy and spectroscopy (STM/STS) studies of the tMoTe<sub>2</sub> moiré superlattice, with twist angles ranging from about 2.3° to 2.8°. We developed a contact-STM mode to apply pressure on tMoTe<sub>2</sub> and observed a phase transition from band insulator to metal of tMoTe<sub>2</sub> under pressure at the charge neutrality point. STM imaging reveals a pronounced in-plane lattice reconstruction with periodic strain redistribution in the tMoTe<sub>2</sub>, which serves as gauge fields for generating topological moiré bands. Importantly, the electronic states of the low-energy moiré flat bands primarily concentrate at the XM and MX regions as revealed by STS imaging. Such spatial distributions are nicely reproduced by our first principal calculations with a large-scale basis, suggesting the low-energy moiré flat bands are formed through the hybridization of K valley bands of the top layer and K' valley bands of the bottom layer. Overall, our findings provide compelling real-space evidence of electronic structure under pressure and topological flat bands of tMoTe<sub>2</sub>, paving the way for further STM/STS investigations of correlated topological states within the topological flat band in gate-tunable tMoTe<sub>2</sub> devices.

## Introduction

Unlike in twisted graphene moiré systems, the flat moiré bands of semiconducting transition metal dichalcogenide (TMDC) moiré systems can be well described by the two-dimensional electron gas model under a spatial modulated potential<sup>33,34</sup>. For TMDC moiré heterobilayer and twisted homobilayer with layer asymmetry, the isolated low-energy flat bands can effectively simulate the Hubbard physics on a triangular lattice<sup>33,34</sup>. The moiré flat bands and strong correlation effects in such systems have also been visualized by previous STM/STS studies<sup>35-46</sup>. On the other hand, for band-aligned twisted homobilayer TMDC or heterobilayers TMDC moiré systems, nontrivial band topology can arise from the hybridization of two sets of moiré flat band from different layer<sup>5,6</sup>. In real space, the low-energy physics can be described by the hopping of carriers on a layer-pseudospin skyrmion lattice, where the layer polarization of wavefunctions is spatially modulated. To date, topological flat bands have been experimentally realized in WSe<sub>2</sub>/MoTe<sub>2</sub> heterobilayer<sup>10-12</sup>, tMoTe<sub>2</sub><sup>13-22</sup>, and twisted bilayer WSe<sub>2</sub> (tWSe<sub>2</sub>)<sup>23,24</sup>. Abundant topological quantum phases, such as the integer/fractional quantum anomalous Hall effect and the integer/fractional quantum spin Hall effect, have been observed in these systems. Importantly, these topological quantum phenomena turn out to be highly sensitively on the details of moiré superlattices, such as the stacking order, moiré wavelength (twisted angles), atomic lattice reconstruction effects, inter-layer pressure, etc. However, the direct atomic-level

characterization of the topological moiré flat bands of TMDc moiré systems in real-space remains elusive, impeding a comprehensive understanding of their microscopic nature.

In this study, we performed STM/STS studies on natural bilayer MoTe<sub>2</sub> and tMoTe<sub>2</sub> with twist angles ranging from approximately 2.3° to 2.8°. Despite being the only TMDc material that exhibits the FQAH state, STM/STS studies of tMoTe<sub>2</sub> has not been reported before. This can be partially attributed to the challenge posed by the instability of MoTe<sub>2</sub> in ambient conditions. To address this challenge, we used a monolayer of h-BN as a protective layer to preserve the intrinsic properties of the MoTe<sub>2</sub> flake while facilitating electron tunneling between the STM tip and the tMoTe<sub>2</sub>. Through this experimental setup, we have developed a contact-STM mode to apply pressures on tMoTe<sub>2</sub> by STM tip and revealed phase transitions from trivial band insulator to metal at the charge neutrality point. Additionally, we have successfully obtained real-space evidence of lattice reconstructions in tMoTe<sub>2</sub>, where reconstructed MX and XM regions are distinctly separated by domain walls. By measuring STS imaging at different energies, we gained insights into the local density of states (LDOS) of both  $\Gamma$  and K valley moiré flat bands. The low energy electronic states exhibit a pronounced LDOS intensity primarily concentrating at the XM and MX regions. These observations are consistent with first-principle calculation results, providing direct evidence of the microscopic origin of the nontrivial band topology in tMoTe<sub>2</sub>.

### **Characterizations of moiré superlattice and lattice reconstructions in tMoTe<sub>2</sub>**

The schematic of our tMoTe<sub>2</sub> device for STM measurements is depicted in Fig. 1a. Exfoliated graphite with the thickness of a few nanometers is utilized as the substrate and electrode for tunneling measurements. Furthermore, to prevent the degradation of air-sensitive tMoTe<sub>2</sub> flake while enabling STM experiments, a monolayer of hexagonal boron nitride (h-BN) is used as the capping layer. Detailed device fabrication processes are described in Methods and Extended Data Fig. 1. To achieve an atomically clean surface suitable for STM imaging, we employ contact mode atomic force microscope (AFM) scanning to sweep away any residual contaminants from the h-BN surface. The efficacy of this sweeping procedure is confirmed through STM imaging, which demonstrates the attainment of a micrometer-sized clean area (Extended Data Fig. 2).

When two layers of MoTe<sub>2</sub> are twisted by a small angle, the long period moiré superlattice is formed with three high-symmetry stackings, denoting as MM, MX, and XM, as depicted in Fig. 1b and 1c. Although the effect of period moiré potential can be understood by considering a rigid lattice structure with continuous variation in stacking configurations<sup>5,6</sup>, the atomically inter- and intra-lattice reconstructions can profoundly influence the moiré band structure and topology. We performed large-scale DFT

calculations to address the lattice relaxation effect of tMoTe<sub>2</sub> with a twist angle of  $\theta = 2.65^\circ$ . The calculation results, illustrated in Fig. 1d, reveal an out-of-plane corrugation induced by inter-lattice interactions, with the MM region elevated by 0.42 Å compared to the XM region, and the XM regions is slightly lower by 0.02 Å than the MX regions. Additionally, the intralayer strain exhibits a helical chirality, as shown in Fig. 1e, leading to the generation of a substantial pseudomagnetic field. Such lattice reconstructions have been considered to be crucial for stabilizing the topological flat band in small-angle-twisted MoTe<sub>2</sub><sup>28</sup>. The calculated band structure including the lattice reconstruction effects is shown in Fig. 1f.

STM measurements were performed on two tMoTe<sub>2</sub> devices with similar twist angles (about 2.3°-2.8°). As demonstrated in Fig. 1f, the STM imaging unveils a moiré period of 8.87/8.05/7.79 nm (corresponding to a twist angle of approximately 2.5°) with a uniaxial strain of  $\epsilon=0.53\%$  (Methods). The STM topographic imaging essentially resembles the key features of the lattice reconstructions predicted by DFT calculations, showing that XM/MX regions with reduced height are separated by domain walls and MM regions. It is important to note that STM topographic imaging captures both structural and electronic contributions (Extended Data Fig. 3). For STM imaging acquired at high bias voltage, it averages the spatial electronic contribution by integrating all the density of states from Fermi level to the applied bias voltage, and reflects dominated spatial structural contributions.

### **Pressure-induced phase transition from band insulator to metal of tMoTe<sub>2</sub> at charge neutrality**

We conducted a comprehensive investigation of the high-energy electronic structure of bilayer MoTe<sub>2</sub> and tMoTe<sub>2</sub> using a combination of DFT calculations and STS measurements (Methods). The DFT-calculated electronic structure (Extended Data Fig. 4) indicates that bilayer MoTe<sub>2</sub> is an indirect semiconductor with a band gap of approximately 0.95 eV. The differential conductance ( $dI/dV$ ) spectra from STS measurements reveal a band gap of approximately 1.37 eV for bilayer MoTe<sub>2</sub>. We observed that the local density of states (LDOS) intensity from the K bands is relatively weak, necessitating a large tunneling current setpoint to resolve the states. This weak intensity is attributed to the large in-plane momentum of the K-valley states, which decays quickly towards the vacuum<sup>37-40</sup>.

The stacking of two MoTe<sub>2</sub> layers with a small twist angle creates a mini moiré Brillouin zone near the K points of the monolayer Brillouin zones with site-dependent LDOS distributions as modulated by moiré superlattice. The calculated total DOS of tMoTe<sub>2</sub> closely resembles that of bilayer MoTe<sub>2</sub>, although it exhibits enhanced fine features due to the presence of the moiré superlattice (Extended Data Fig. 5).

Experimentally, site-dependent  $dI/dV$  spectra exhibit characteristics similar to those observed in bilayer  $\text{MoTe}_2$ , with slight variations in peak intensity and positions across different regions of the moiré superlattice, as shown in Fig. 2a and 2b. An energy gap of approximately 1.56 V is observed at the MX and XM region, and a gap of 1.67 V is observed at the MM region.

The electronic band gap of TMDc materials is highly sensitive to pressure variations. Our experimental setup allows for STM/STS measurements in a contact mode (contact-STM) due to the presence of a dielectric h-BN layer in the STM junction. Concurrently, forces between the STM tip and the  $\text{tMoTe}_2$  sample can be applied using scanner piezoceramics (Methods), as illustrated in Fig. 2c. Using contact-STM, we investigate the effects of pressure-induced band gap evolution. As depicted in Fig. 2d-f, a continuous suppression of the  $\text{tMoTe}_2$  band gap from about 1.5 eV to nearly zero is observed with increasing force between the tip and the  $\text{tMoTe}_2$ . Notably, we observe a phase transition from a band insulator to a possible topological insulator, characterized by band inversion and the avoidance of band crossing at the Fermi level. This band inversion occurs in the first few low-lying bands, as indicated by red arrows in Fig. 2f. With further increased force, the band gap eventually decreases to zero, resulting in a metallic state, as shown in Fig. 2d-e.

We conducted contact-STM measurements at various high-symmetry regions of  $\text{tMoTe}_2$  (Extended Data Fig. 6). The phenomena of gap suppression, band inversion, and gap closure were consistently observed across all regions, with slight variations attributed to the spatial modulation by moiré superlattices. The noninvasive nature of these contact-STM measurements was confirmed by comparing STM images taken before and after the measurements (Extended Data Fig. 6). For comparative analysis, the pressure-induced gap suppression of bilayer  $\text{MoTe}_2$  was also investigated. In bilayer  $\text{MoTe}_2$ , we observed similar phase transition from band insulator to topological insulator and eventually to a metallic state (Extended Data Fig. 6).

DFT calculations indicate that both applied pressure and electric field can suppress the band gap of bilayer  $\text{MoTe}_2$ . As illustrated in Fig. 2g, the calculated band gap continuously decreases with reduced interlayer distance (increased pressure), reaching zero at an interlayer distance of approximately 6.3 Å, corresponding to a pressure of approximately 0.8 GPa. Such pressure is readily achievable using a sharp STM tip with a diameter of tens of nanometers. Unlike the continuous suppression observed under pressure, DFT calculations suggest the band gap decreases slowly with increased electric field, but abruptly goes to zero at a critical electric field of approximately 7 V/nm, which is far beyond the achievable electric field range in experiments (Extended Data Fig. 6). To further ensure that the band gap suppression is not due to the electric field, we replaced the hard tungsten tip with a soft lead tip (with similar work function

compared to tungsten) and did not observe the gap closure behavior but observed the gap suppression, in consistent with DFT calculations (Extended Data Fig. 6). We calculated the band structure of MoTe<sub>2</sub> under pressure and found that the top valence band will touch the bottom conduction band, giving a band inversion with non-trivial topological character (Extended Data Fig. 7).

### **Electronic structure of deep moiré flat bands at both the $\Gamma$ and K valley**

The moiré superlattice reconstruction significantly influences the electronic properties of the moiré flat bands. To further investigate this, we performed zoom-in constant-height STS measurements to resolve the moiré flat bands near the valence band edge. As illustrated in Fig. 3a, four representative  $dI/dV$  spectra, taken on different high-symmetry sites, reveal site-dependent LDOS distributions, with peaks at -0.71 V on the XM site, -0.74 V on the MX site, -0.77 V on the domain wall (DW) site, and -0.87 V on the MM site. To gain further insights into these site-dependent behaviors, a constant-height  $dI/dV$  line plot was obtained along the high-symmetry direction in real space (Fig. 3b). The states at XM and MX sites gradually extend to the MM and DW regions with increased bias. This observation indicates that lattice relaxation isolates the XM and MX regions by the DW and MM regions. The hybridization of the MX states of the top layer with the XM states of the bottom layer form moiré bands with a honeycomb lattice LDOS distributions.

As illustrated in Fig. 3c, the spatial  $dI/dV$  map captured at -0.71 V reveals such honeycomb lattice-like LDOS distributions localized at the MX/XM regions. The LDOS intensities are predominantly concentrated at the three XM regions, while significantly weaker at the MX regions. At a slightly higher energy of -0.73 V, the LDOS intensity at the XM/MX center is weaker than that in the outer areas, forming hollow honeycomb-like features. At a bias of -0.81 V, the LDOS intensities are primarily located at the domain walls, and at a bias of -0.88 V, they are concentrated at the MM regions. We attribute these states to deeper moiré flat bands originating from both the K and  $\Gamma$  valleys (see detailed discussion in next section), which are effectively captured by our DFT calculations (Extended Data Fig. 8).

We observed that the energy position and energy splitting between the XM and MX regions are highly sensitive to the details of the STM tip. STS  $dI/dV$  spectra taken at two regions with similar strain but with different tip apexes exhibit distinct peak positions and energy splitting at the XM and MX regions (Extended Data Fig. 9, 10). Therefore, we attribute this splitting to a tip-induced electric field effect.

### **Electronic structure of the low-energy topological moiré flat bands at K valley**

Due to lattice relaxation in MoTe<sub>2</sub>, the low-energy moiré valence bands originate from the  $\pm K$  valley rather than the  $\Gamma$  valley<sup>7</sup>. The topmost moiré flat band at the K valley is topologically non-trivial, giving rise to the observed FQAH effect in tMoTe<sub>2</sub>. We present comprehensive calculations and STS spectroscopy to differentiate the moiré flat band from the K valley from that of the  $\Gamma$  valley. We began by calculating the wavefunction contributions of the K- and  $\Gamma$ -point states. Our calculations indicate that the  $\Gamma$ -point states originate from the  $d_{z^2}$  orbitals of Mo and Te (Extended Data Fig. 11), which possess out-of-plane momentum and therefore decay slowly outside the MoTe<sub>2</sub> layer. In contrast, the K-point states originate from the in-plane  $d_{xy}$  orbitals of Mo and the  $p_x$  and  $p_y$  orbitals of Te (Extended Data Fig. 11). These wavefunctions have large in-plane momentum and decay rapidly outside the MoTe<sub>2</sub> layer.

We performed DFT calculations to address the energy position of K and  $\Gamma$  valley moiré flat bands as shown in Fig. 4a-b. For all the twisted angles, the topmost K valley moiré flat band lies closer to Fermi level, and the energy difference between the topmost K valley and  $\Gamma$  valley moiré flat bands decreases with reduced twist angle with values around 70 meV for twist angle around 2.65°, due to the reduction of K-valley moiré band width.

The rapid decay of K-valley states outside the MoTe<sub>2</sub> layer poses significant challenges for STS measurements, necessitating the use of a very sharp STM tip to minimize the screening effect. To produce such a sharp tip, a tungsten wire with a diameter of 25  $\mu\text{m}$  was etched, and the tip apex was further shaped by in-situ field emission by applying a voltage of 200 V between the tungsten tip and the Cu (111) surface. The typical spectra obtained using this sharp tip are shown in Fig. 4c. The previously observed peaks at -0.68 V and -0.74 V on the XM and MX regions (Fig. 3a) shift to -0.95 V, with peak positions at XM and MX nearly degenerate. This observation confirms that such sharp tip induced screening effect is much weaker than typical STM tips.

Using such measurements, we observe a shallow shoulder on the top MX sites at a bias ranging from -0.7 V to -0.9 V (Fig. 4d). Spatial STS mapping reveals that the LDOS is predominantly located at the MX regions, becoming more extended with increased bias (Fig. 4f-h). These spatial distributions are well reproduced by DFT calculations using the topmost moiré flat bands from the K valley (Fig. 4i-l). At a bias of -0.96 V, the LDOS intensity increases dramatically, forming a honeycomb pattern, which is also accurately reproduced by DFT calculations using the moiré bands from the  $\Gamma$  valley. In summary, our STS measurements confirm that the K-valley moiré flat bands lie above the  $\Gamma$ -valley moiré flat bands. The observed fast decay behavior and spatial distributions are in excellent agreement with the DFT calculations.

## Conclusions and Outlook

We present a comprehensive real-space study of an h-BN encapsulated tMoTe<sub>2</sub> sample, revealing lattice relaxation, band gap characteristics, and the low-energy moiré flat bands from both the  $\Gamma$ -valley and K-valley. These observations are in excellent agreement with our large-basis DFT calculations. Additionally, employing this device setup, we develop a contact-STM mode to investigate the effects of pressure on the electronic structure, introducing a novel approach that has been largely overlooked in experimental studies thus far. Using this setup, we successfully observed the phase transition from band insulator to topological insulator and eventually to a metallic state with increasing pressure. Given the versatility of tMoTe<sub>2</sub>, our findings open up further opportunities to study pressure-induced quantum phases and to visualize exotic quantum phases, such as FQAH anyons, in real space.

**Additional Notes:** During the preparation of this manuscript, we become aware of a recent work that also reports the STM/STS study on tMoTe<sub>2</sub><sup>47</sup>.

## References

1. Balents, L., Dean, C. R., Efetov, D. K. & Young A. F. Superconductivity and strong correlations in moiré flat bands. *Nat. Phys.* **16**, 725-733 (2020).
2. Kennes, D. M. et al. Moiré heterostructures as a condensed-matter quantum simulator. *Nat. Phys.* **17**, 155-163 (2021).
3. Mak, K. F. & Shan, J. Semiconductor moiré materials. *Nat. Nanotech.* **17**, 686-695 (2022).
4. Morales-Durán, N., Shi, J. & MacDonald, A.H. Fractionalized electrons in moiré materials. *Nat Rev Phys* **6**, 349–351 (2024)
5. Wu, F., Lovorn, T., Tutuc, E., Martin, I. & MacDonald, A. H. Topological insulators in twisted transition metal dichalcogenide homobilayers. *Phys. Rev. Lett.* **122**, 086402 (2019).
6. Yu, H., Chen, M. & Yao, W. Giant magnetic field from moiré induced Berry phase in homobilayer semiconductors. *Natl. Sci. Rev.* **7**, 12-20 (2020).
7. Devakul, T., Crépel, V., Zhang, Y. & Fu, L. Magic in twisted transition metal dichalcogenide bilayers. *Nat. Commun.* **12**, 6730 (2021).
8. Li, H., Kumar, U., Sun, K. & Lin, S. Z. Spontaneous fractional Chern insulators in transition metal dichalcogenide moiré superlattices. *Phys. Rev. Res.* **3**, L032070 (2021).
9. Crépel, V. & Fu, L. Anomalous Hall metal and fractional Chern insulator in twisted transition metal dichalcogenides. *Phys. Rev. B* **107**, L201109 (2023).
10. Li, T. et al. Quantum anomalous Hall effect from intertwined moiré bands. *Nature*



**600**, 641-646 (2021).

11. Zhao, W. *et al.* Realization of the Haldane Chern insulator in a moiré lattice. *Nat. Phys.* **20**, 275–280 (2024).
12. Tao, Z. *et al.* Valley-coherent quantum anomalous Hall state in AB-stacked MoTe<sub>2</sub>/WSe<sub>2</sub> bilayers. *Phys. Rev. X* **14**, 011004 (2024).
13. Anderson, E. *et al.* Programming correlated magnetic states with gate-controlled moiré geometry. *Science* **381**, 325-330 (2023).
14. Cai, J. *et al.* Signatures of fractional quantum anomalous Hall states in twisted MoTe<sub>2</sub>. *Nature* **622**, 63–68 (2023).
15. Zeng, Y. *et al.* Thermodynamic evidence of fractional Chern insulator in moiré MoTe<sub>2</sub>. *Nature* **622**, 69–73 (2023).
16. Park, H. *et al.* Observation of fractionally quantized anomalous Hall effect. *Nature* **622**, 74–79 (2023).
17. Xu, F. *et al.* Observation of integer and fractional quantum anomalous Hall effects in twisted bilayer MoTe<sub>2</sub>. *Phys. Rev. X* **13**, 031037 (2023).
18. Kang, K. *et al.* Evidence of the fractional quantum spin Hall effect in moiré MoTe<sub>2</sub>. *Nature* **628**, 522–526 (2024).
19. Ji, Z. *et al.* Local probe of bulk and edge states in a fractional Chern insulator. Preprint at <https://arxiv.org/abs/2404.07157> (2024).
20. Redekop, E. *et al.* Direct magnetic imaging of fractional Chern insulators in twisted MoTe<sub>2</sub> with a superconducting sensor. Preprint at <https://arxiv.org/abs/2405.10269> (2024).
21. Xu, F. *et al.* Interplay between topology and correlations in the second moiré band of twisted bilayer MoTe<sub>2</sub>. Preprint at <https://arxiv.org/abs/2406.09687> (2024).
22. Park, H. *et al.* Ferromagnetism and Topology of the Higher Flat Band in a Fractional Chern Insulator. Preprint at <https://arxiv.org/abs/2406.09591> (2024).
23. Kang, K. *et al.* Observation of the double quantum spin Hall phase in moiré WSe<sub>2</sub>. Preprint at <https://arxiv.org/abs/2402.04196> (2024).
24. Foutty, B. A. *et al.* Mapping twist-tuned multiband topology in bilayer WSe<sub>2</sub>. *Science* **384**, 343-347 (2024).
25. Morales-Durán, N. *et al.* Pressure-enhanced fractional Chern insulators along a magic line in moiré transition metal dichalcogenides. *Phys. Rev. Res.* **5**, L032022 (2023).
26. Reddy, A. P., Alsallom, F., Zhang, Y., Devakul, T. & Fu, L. Fractional quantum anomalous Hall states in twisted bilayer MoTe<sub>2</sub> and WSe<sub>2</sub>. *Phys. Rev. B* **108**, 085117 (2023).
27. Wang, C. *et al.* Fractional Chern insulator in twisted bilayer MoTe<sub>2</sub>. *Phys. Rev. Lett.* **132**, 036501 (2024).
28. Mao, N. *et al.* Transfer learning electronic structure and continuum model for

- twisted bilayer MoTe<sub>2</sub>. Preprint at <https://arxiv.org/abs/2311.07533> (2023).
29. Zhang, X. W. *et al.* Polarization-driven band topology evolution in twisted MoTe<sub>2</sub> and WSe<sub>2</sub>. *Nat Commun* **15**, 4223 (2024).
  30. Jia, Y. *et al.* Moiré fractional Chern insulators. I. First-principles calculations and continuum models of twisted bilayer MoTe<sub>2</sub>. *Phys. Rev. B* **109**, 205121 (2024).
  31. Xu, C., Li, J., Xu, Y., Bi, Z. & Zhang, Y. Maximally localized Wannier functions, interaction models, and fractional quantum anomalous Hall effect in twisted bilayer MoTe<sub>2</sub>. *Proc. Natl. Acad. Sci. U.S.A.* **121**, e2316749121 (2024).
  32. Morales-Durán, N., Wei, N., Shi, J. & MacDonald, A. H. Magic angles and fractional Chern insulators in twisted homobilayer transition metal dichalcogenides. *Phys. Rev. Lett.* **132**, 096602 (2024).
  33. Wu, F., Lovorn, T., Tutuc, E. & MacDonald, A. H., Hubbard Model Physics in Transition Metal Dichalcogenide moiré Bands. *Phys. Rev. Lett.* **121**, 026402 (2018).
  34. Zhang, Y., Yuan, N. F. Q. & Fu, L., Moiré quantum chemistry: Charge transfer in transition metal dichalcogenide superlattices. *Phys. Rev. B* **102**, 201115 (2020).
  35. Zhang, C. *et al.* Interlayer couplings, Moiré patterns, and 2D electronic superlattices in MoS<sub>2</sub>/WSe<sub>2</sub> hetero-bilayers. *Sci. Adv.* **3**, e1601459 (2017).
  36. Shabani, S. *et al.* Deep moiré potentials in twisted transition metal dichalcogenide bilayers. *Nat. Phys.* **17**, 720-725 (2021).
  37. Zhang, Z. *et al.* Flat bands in twisted bilayer transition metal dichalcogenides. *Nat. Phys.* **16**, 1093–1096 (2020).
  38. Li, E. *et al.* Lattice reconstruction induced multiple ultra-flat bands in twisted bilayer WSe<sub>2</sub>. *Nat. Commun.* **12**, 5601 (2021).
  39. Li, H. *et al.* Imaging moiré flat bands in three-dimensional reconstructed WSe<sub>2</sub>/WS<sub>2</sub> superlattices. *Nat. Mater.* **20**, 945-950 (2021).
  40. Pei, D. *et al.* Observation of  $\Gamma$ -Valley Moiré Bands and Emergent Hexagonal Lattice in Twisted Transition Metal Dichalcogenides. *Phys. Rev. X* **12**, 021065 (2022).
  41. Li, H. *et al.* Imaging two-dimensional generalized Wigner crystals. *Nature* **597**, 650-654 (2021).
  42. Li, H. *et al.* Imaging local discharge cascades for correlated electrons in WS<sub>2</sub>/WSe<sub>2</sub> moiré superlattices. *Nat. Phys.* **17**, 1114-1119 (2021).
  43. Tilak, N. *et al.* Moiré Potential, Lattice Relaxation, and Layer Polarization in Marginally Twisted MoS<sub>2</sub> Bilayers. *Nano Lett.* **23** (1), 73-81 (2023).
  44. Li, H. *et al.* Imaging moiré excited states with photocurrent tunnelling microscopy. *Nat. Mater.* **23**, 633-638 (2024).
  45. Li, H. *et al.* Mapping charge excitations in generalized Wigner crystals. *Nat. Nano.* **19**, 618-638 (2024).

46. Li, H. *et al.* Wigner Molecular Crystals from Multi-electron Moiré Artificial Atoms. Preprint at <https://arxiv.org/abs/2312.07607v1> (2023).
47. Thompson, E. *et al.* Visualizing the microscopic origins of topology in twisted molybdenum ditelluride. Preprint at <https://arxiv.org/abs/2405.19308> (2024).

## Methods

### Device fabrications

The tMoTe<sub>2</sub> stacks for STM/STS measurements were fabricated using the standard dry transfer method<sup>48</sup> (Extended Data Fig. 1) in a nitrogen-filled glovebox to prevent the degradation of the MoTe<sub>2</sub>. First, we prepared electrodes (Ti/Au 10 nm/60 nm) on Si/SiO<sub>2</sub> substrates using e-beam lithography and e-beam evaporation. Then, monolayer h-BN, monolayer MoTe<sub>2</sub>, graphite (~ 3-5 nm), and h-BN (~10-20 nm) were mechanically exfoliated onto Si/SiO<sub>2</sub> substrates and identified via optical contrast. A monolayer h-BN was initially picked by a polycarbonate (PC) film stamp. This monolayer h-BN was then used to pick up half of the monolayer MoTe<sub>2</sub> (which was cut into two pieces with an AFM tip before stacking). The remaining MoTe<sub>2</sub> was picked up after rotating it by a small angle controlled by a mechanic rotator. After picking up the bottom graphite and bottom h-BN layers, the entire stack was released onto the prepatterned Ti/Au electrodes. The monolayer h-BN served as the protection layer for tMoTe<sub>2</sub>. The bottom graphite served as the tunneling electrodes for the STM tip, while the bottom h-BN layer screened inhomogeneities generated by substrate surface roughness. The finished stack was dipped in chloroform, acetone and isopropanol for a few minutes, respectively, to remove the majority of the PC film. Finally, any residual contaminants were cleaned by repeated scanning with an atomic force microscope operated in contact mode (Park NX7, setting contact force ~ 300 nN), in order to obtain an atomically-clean surface for STM/STS measurements. Before measurement, these samples were annealed in ultrahigh vacuum at 150 °C overnight.

### Angle inhomogeneity and strain

The local twist angle and strain of tMoTe<sub>2</sub> are determined using a uniaxial hetero-strain model<sup>49</sup>, which assumes that one layer is uniaxially strained by a percentage  $\varepsilon$  at an angle  $\theta_s$  to one of the MoTe<sub>2</sub> crystal lattices, while the other layer remains unstrained but with a twist angle  $\theta_T$  relative to the first. This model provides three degrees of freedom for the tensile moiré geometry: the moiré twist angle  $\theta_T$ , the heterostrain magnitude  $\varepsilon$ , and the angle of uniaxial strain application  $\theta_s$ . These three variables can be numerically solved by fitting with the experimentally measured three side moiré

wavelengths. In this work, the MoTe<sub>2</sub> Poisson ratio is estimated to be  $\delta = 0.24$ <sup>50</sup>. Additionally, a statistical analysis was conducted on two samples, and the respective twist angle ranges and strain levels are illustrated in Extended Data Fig. 2.

### STM/STS measurements

STS/STM were carried out using a commercial Unisoku Joule-Thomson STM and a commercial Unisoku 1200JT STM system under low temperature (4.8 K) and ultra-high vacuum conditions ( $3 \times 10^{-10}$  mbar). The tungsten tips were calibrated against the surface state of a Cu (111) single crystal or an Ag (111) single crystal. The Pb-functionalized tip was calibrated on Pb (111) grown on the HOPG substrate, exhibiting a distinct superconducting gap. A lock-in amplifier (521 Hz, 3–20 mV modulation) were used to acquire  $dI/dV$  spectra. The STM tip was navigated to samples using the capacitance-guiding technique<sup>51</sup>. The STM images were processed with WSxM software. For contact-STM measurements, we approach the tip slowly to the h-BN surface and record the tunneling current using a FEMTO preamplifier. During the measurements, the feedback loop is switched off, and the voltage of scanning piezoceramics is gradually increased to apply pressure on the sample.

### Theoretical calculation

Our first-principles calculations are based on density functional theory (DFT) as implemented in the open-source package for material explorer (OpenMX)<sup>52</sup> and Vienna Ab initio Simulation Package (VASP)<sup>53</sup>. For the tMoTe<sub>2</sub> with twist angle  $2.65^\circ$  calculated by OpenMX, we adopt the relaxed structure with moiré wavelength  $76.23 \text{ \AA}$ <sup>29</sup> and get the electronic structure under self-consistent criterion of  $7 \times 10^{-4}$  eV. In the DOS and LDOS calculation in tMoTe<sub>2</sub>, an  $81 \times 81 \times 1$  Monkhorst-Pack k-point mesh is applied to sample the Brillouin zone (BZ) and the gaussian smearing of energy is chosen to be 0.007 eV. The valley-resolved DOS is generated by considering the summation of projected components of in-plane atomic orbitals as K valley's contribution and summation of out-of-plane ones as  $\Gamma$  valley's contribution. For the bilayer AB-stacking MoTe<sub>2</sub> calculated by VASP, we adopt an in-plane lattice constant of  $3.52 \text{ \AA}$  and apply two different van der Waals (vdW) corrections: DFT-D2 and DFT-dDsC. The ionic potential is treated using the projector augmented wave (PAW) method. Exchange-correlation interactions are handled with the Perdew-Burke-Ernzerhof (PBE) functional within the generalized gradient approximation (GGA). We employ a plane-wave basis set truncated at a cutoff energy of 600 eV. Convergence thresholds are meticulously set at  $0.001 \text{ eV/\AA}$  for forces and  $10^{-6}$  eV for total energy. To sample the three-dimensional BZ, we use an  $11 \times 11 \times 1$  Monkhorst-Pack k-point mesh.

48. Wang, L. *et al.* One-dimensional electrical contact to a two-dimensional material. *Science* **342**, 614–617 (2013).
49. Kerelsky, A. *et al.* Maximized electron interactions at the magic angle in twisted bilayer graphene. *Nature* **572**, 95–100 (2019).
50. Kang, J., Tongay, S., Zhou, J., Li, J., Wu, J., Band offsets and heterostructures of two-dimensional semiconductors. *Appl. Phys. Lett.* **102** (1): 012111 (2013).
51. Li, G., Luican, A., Andrei, E. Y., Self-navigation of a scanning tunneling microscope tip toward a micron-sized graphene sample. *Rev. Sci. Instrum.*, **82**(7), 073701 (2011).
52. Ozaki, T. Variationally optimized atomic orbitals for large-scale electronic structures. *Phys. Rev. B* **67**, 155108 (2003).
53. Kresse, G. & Furthmüller, J. Efficient iterative schemes for ab initio total-energy calculations using a plane-wave basis set. *Phys. Rev. B* **54**, 11169–11186 (1996).

### **Acknowledgement**

This work is supported by the National Key R&D Program of China (Nos. 2022YFA1405400, 2022YFA1402401, 2022YFA1402404, 2021YFA1401400, 2022YFA1402702, 2021YFA1400100, 2020YFA0309000, 2019YFA0308600, 2019YFA0308600), the National Natural Science Foundation of China (Nos. 12350403, 12174249, 12174250, 12141404, 92265102, 12374045, 92365302, 22325203, 92265105, 92065201, 12074247, 12174252, 22272050, 21925201), the Innovation Program for Quantum Science and Technology (Nos. 2021ZD0302600 and 2021ZD0302500), the Natural Science Foundation of Shanghai (No. 22ZR1430900). T.L. and X.L. acknowledge the Shanghai Jiao Tong University 2030 Initiative Program. X.L. acknowledges the Pujiang Talent Program 22PJ1406700. T.L. acknowledges the Yangyang Development Fund. Yang Zhang acknowledges support from AI-Tennessee and Max Planck partner lab grant. K.W. and T.T. acknowledge support from the JSPS KAKENHI (Nos. 21H05233 and 23H02052) and World Premier International Research Center Initiative (WPI), MEXT, Japan.

### **Author contributions**

S.W. and T.L. designed and supervised the experiment. Y.G. and S.J. fabricated the devices. Y.L. and C.L. performed the STM/STS measurements. L.L., D.G., Y.L., H.Z., C.L., J.J., X.L. S.W., T.L. and Y.Z. analyzed the data. T.B., N.M. W.D. and Y.Z. performed theoretical studies. K.W. and T.T. grew the bulk h-BN crystals. Y.L., S.W.,

T.L. and Y.Z. wrote the manuscript. All authors discussed the results and commented on the manuscript.

### **Competing interests**

The authors declare no competing financial interests.

## Main Figures

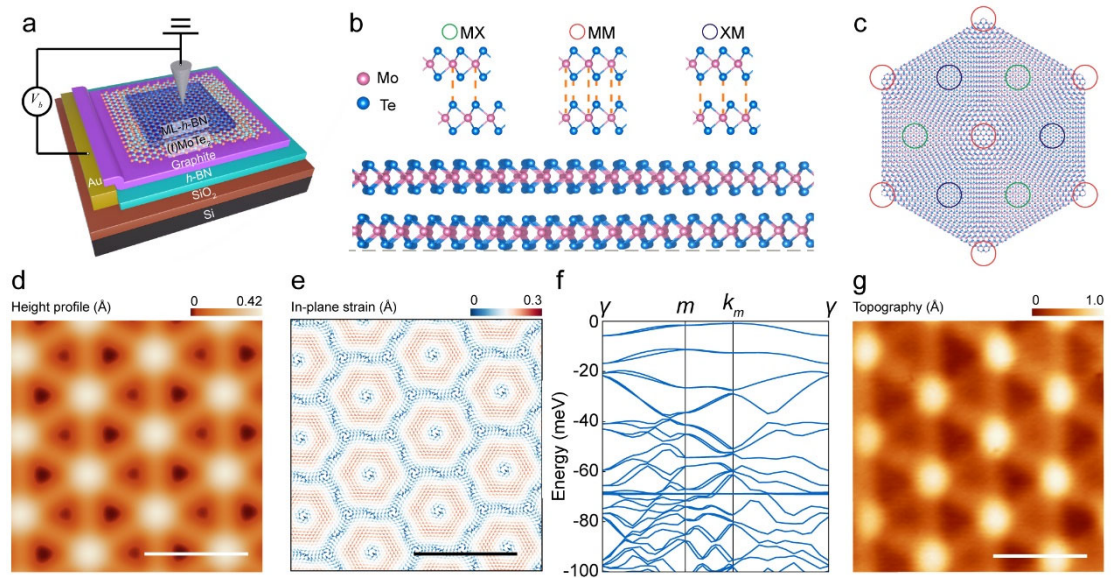


**Fig. 1. Device structure and lattice relaxation of tMoTe<sub>2</sub>.** **a**, Schematic of the tMoTe<sub>2</sub> device for STM/STS measurements. A monolayer of h-BN is used to protect the air-sensitive MoTe<sub>2</sub> flake while facilitating electron tunneling. **b,c**, Side view (**b**) and top view (**c**) of the schematic moiré superlattice of tMoTe<sub>2</sub>. High symmetry stackings are highlighted by circles. **d,e**, Theoretical calculation results of height profile (**d**) and in-plane strain distribution (**e**) of 2.65° tMoTe<sub>2</sub>. **f**, The calculated band structure of 2.65° tMoTe<sub>2</sub> by incorporating the lattice relaxations. **g**, Experimental STM topography of about 2.5° tMoTe<sub>2</sub> (device A,  $V_{\text{bias}} = -1.5$  V and  $I = 1$  nA).

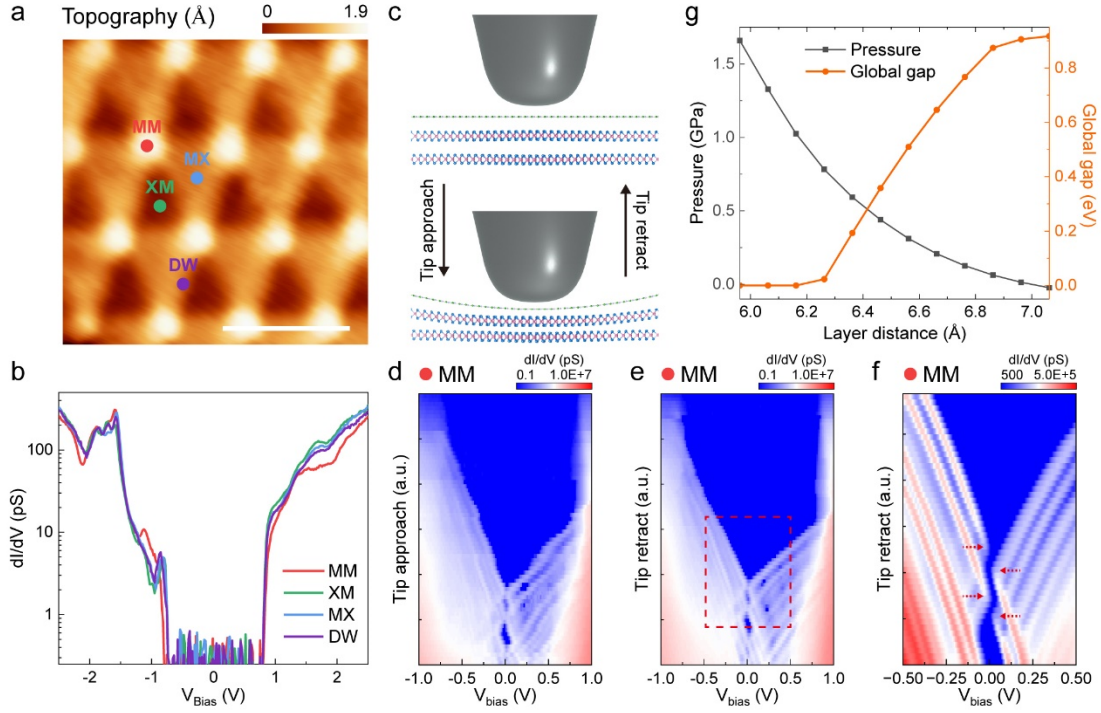


**Fig. 2. Pressure-induced phase transition from band insulator to metal.** **a**, STM topography of a tMoTe<sub>2</sub> region with  $\theta \approx 2.8^\circ$  (device B,  $V_{\text{bias}} = -1.6$  V and  $I = 50$  pA). High symmetry stackings are marked by dots. **b**, STS  $dI/dV$  spectra taken on the sites marked in **(a)**. (Bias Modulation: 20 mV) **c**, Schematic showing the contact-STM measurements. Due to the presence of h-BN monolayer, the STM tip can be used to apply pressure on the sample while allowing STS measurements. **d,e**, STS  $dI/dV$  spectra plot taken with contact-STM mode recorded during tip-approach process **(d)** and during tip-retract process **(e)** (Bias Modulation: 20 mV). **f**, Zoomed-in  $dI/dV$  spectra plot in the region as marked in **(e)**. The dashed red arrows mark the band inversion regions. **g**, DFT calculated band gap suppression as a function of layer distance and corresponding pressure.



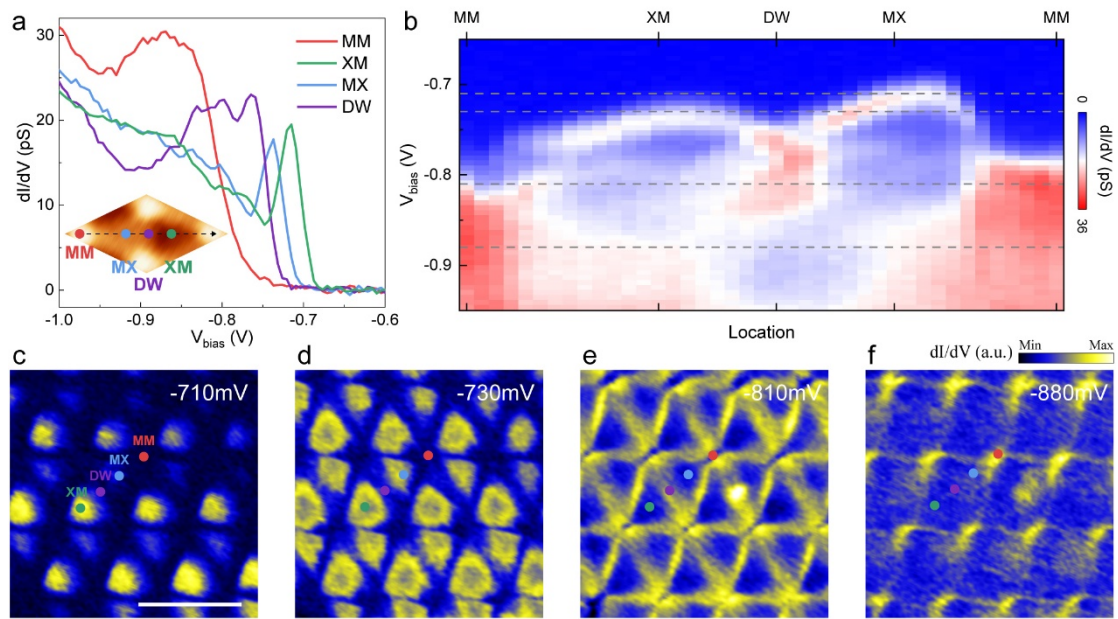


**Fig. 3. STS measurements of the moiré flat bands from both  $\Gamma$  and K valley of tMoTe<sub>2</sub>.** **a**,  $dI/dV$  spectra taken at high-symmetry points on a tMoTe<sub>2</sub> region with  $\theta \approx 2.8^\circ$  (device B). The inset shows the STM topography at the same region with high symmetry stackings marked by colored dots. **b**, 2D plot of line  $dI/dV$  spectra taken along the dashed line in the inset of **(a)**. **c-f**, Constant-height STS mappings taken at different  $V_{\text{bias}}$  as marked by dashed lines in **(b)**. The scale bar is 10 nm. (Bias Modulation: 10 mV)

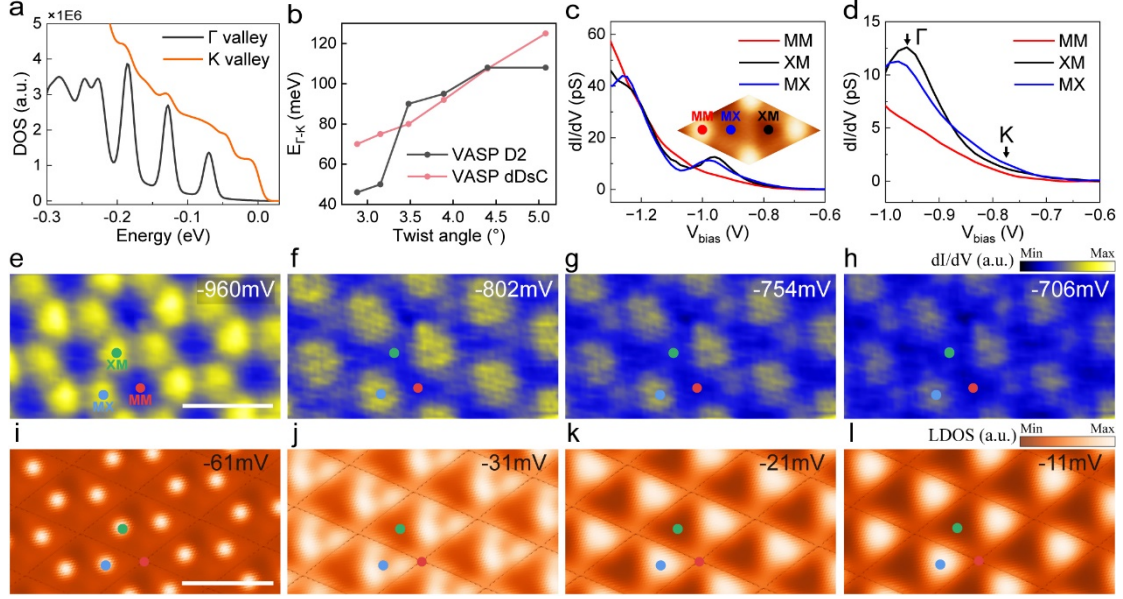
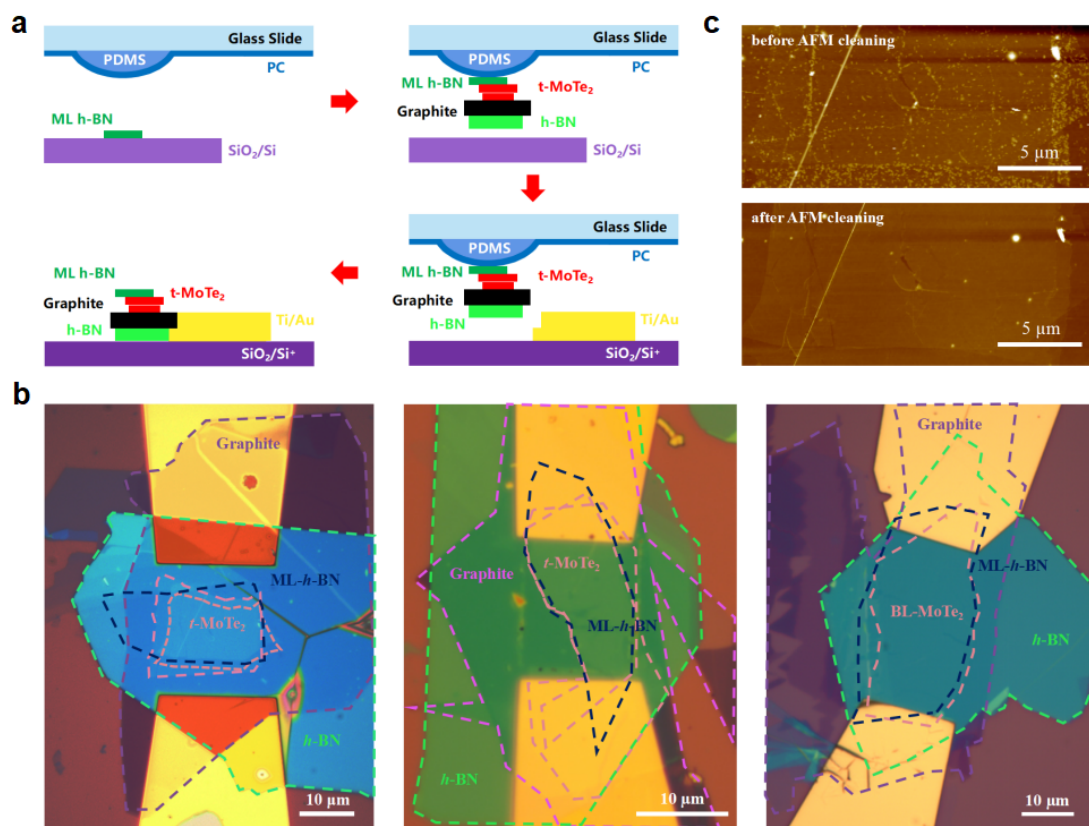
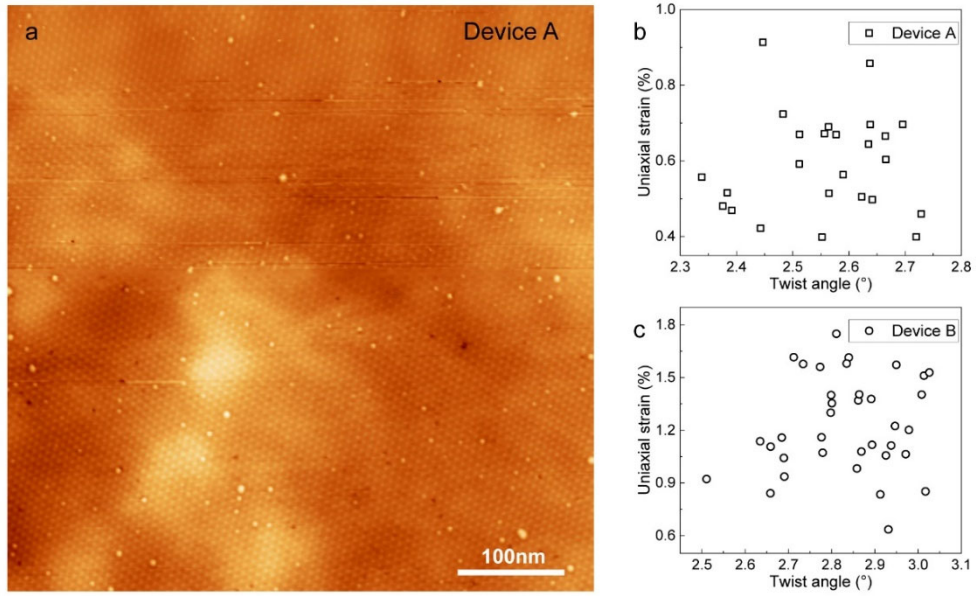


**Fig. 4.** The low-energy topological moiré flat bands from K valley of tMoTe<sub>2</sub>. **a**, DFT calculated DOS spectra of moiré flat bands from the  $\Gamma$  and K valley. The topological moiré flat bands from K valley lie closer to the fermi level than that of  $\Gamma$  Valley. **b**, DFT calculated energy difference between the topmost K-Valley moiré flat band and the topmost  $\Gamma$ -Valley moiré flat band. **c**, STS  $dI/dV$  spectra taken at high-symmetry points, marked by colored dots in the inset STM image, for a tMoTe<sub>2</sub> region with  $\theta \approx 2.5^\circ$  (device A). **d**, Zoomed-in  $dI/dV$  spectra showing the weak shoulder features from K-Valley moiré flat bands, and peak feature from  $\Gamma$ -Valley moiré flat bands. **e-h**, Constant-height STS mappings taken at different  $V_{\text{bias}}$  with scale bar of 10 nm. Bias Modulation: 20 mV. **i-l**, DFT calculated DOS maps of the top layer of  $2.65^\circ$  tMoTe<sub>2</sub> at different energies.

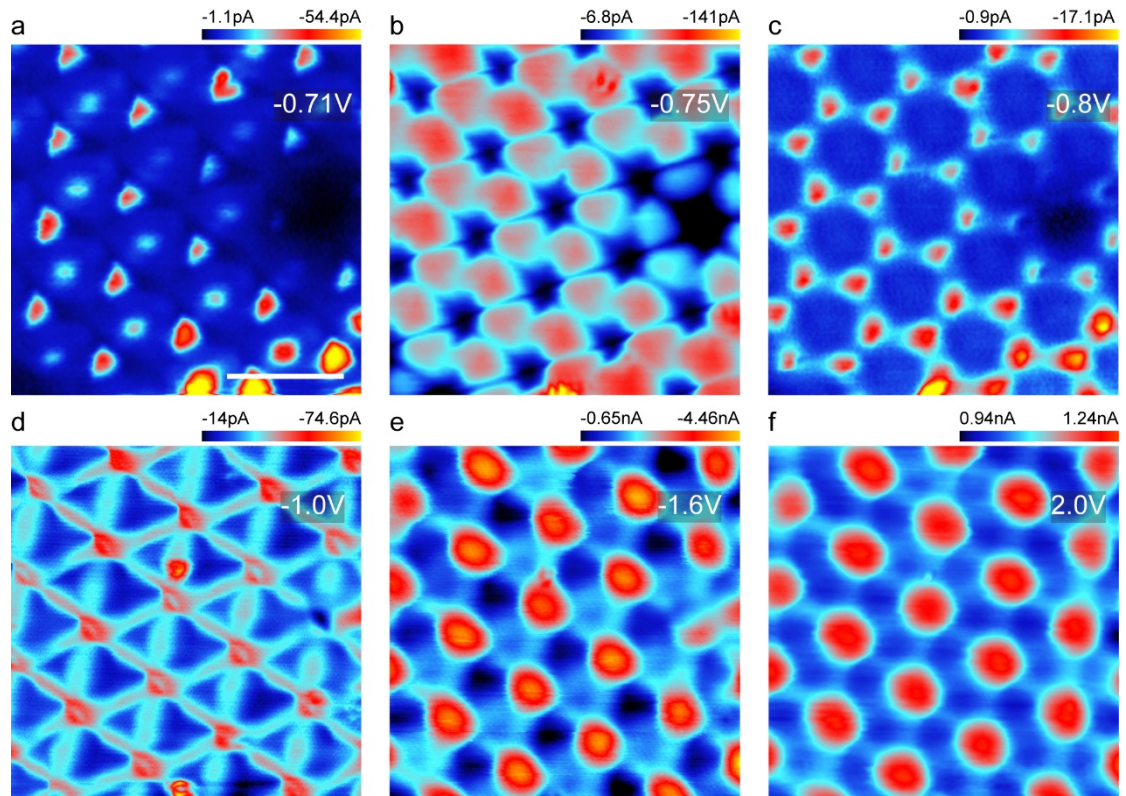
## Extended Data Figures



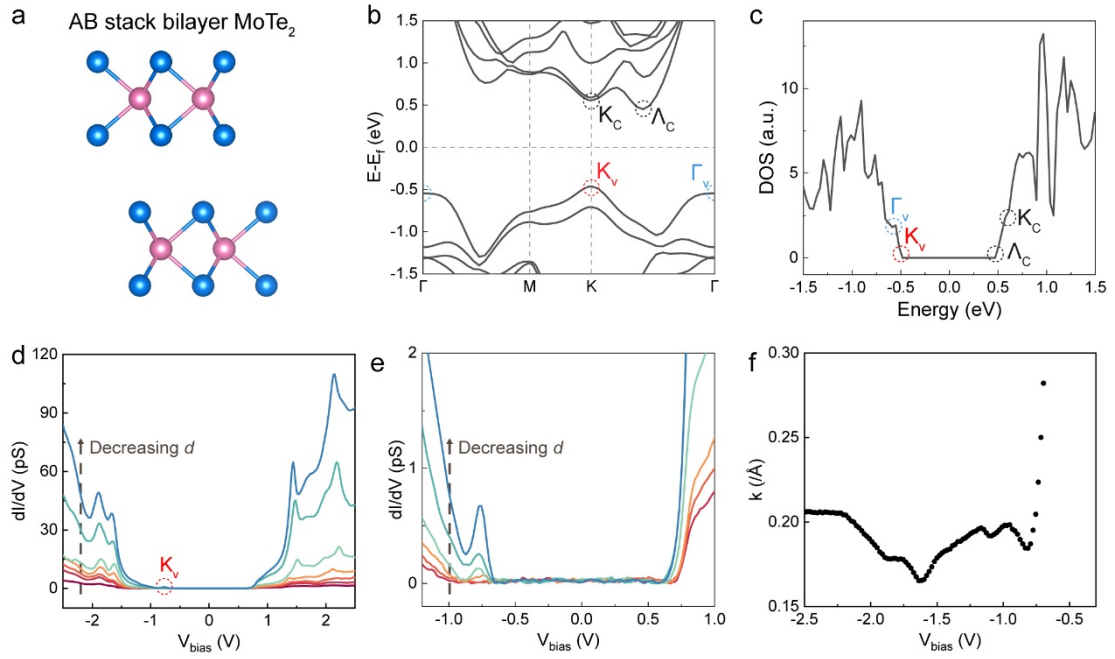
**Extended Data Fig. 1. Device fabrication procedure.** **a**, Schematic of the device fabrication processes (see Methods for details). **b**, Optical micrographs of the tMoTe<sub>2</sub> device A and B, and bilayer MoTe<sub>2</sub> device (from left to right). Pink and blue dashed lines highlight the tMoTe<sub>2</sub> and monolayer h-BN regions; purple and green dashed lines highlight the bottom graphite and bottom h-BN flakes, Scale bars are 10 μm. **c**, AFM topography of the tMoTe<sub>2</sub> device B before and after contact-mode AFM cleaning. Scale bars are 5 μm.



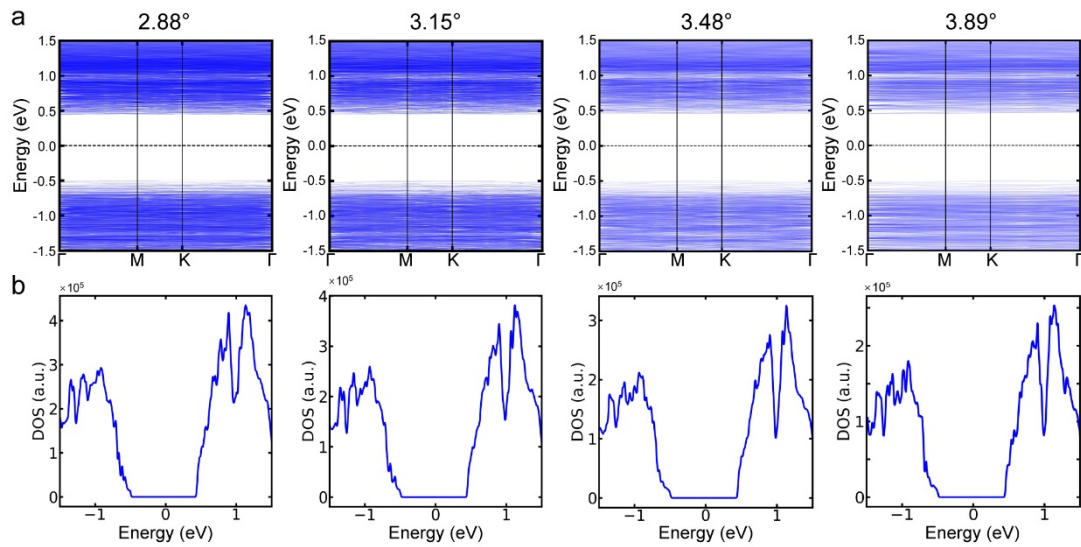
**Extended Data Fig. 2. Large scale STM image of tMoTe<sub>2</sub> Device A sample. a**, STM topography of a tMoTe<sub>2</sub> (Device A,  $V_{\text{bias}} = -2.0$  V and  $I = 145$  pA). The sample is micrometer-size clean with only few point defects. **b,c**, The analyzed uniaxial strain as a function of twist angle of device A (**b**) and device B (**c**).



**Extended Data Fig. 3. Constant-height STM images taken at different bias voltages.** STM topographic imaging captures both structural and electronic contributions, which is sensitive to applied bias. To get the topographic features, we take STM images at large bias voltages (e and f). For STM imaging acquired at high bias voltages, it averages the spatial electronic contribution by integrating all the states from Fermi level to the applied bias voltage, and thus the structure contributions dominant in the high-bias STM imaging. Scale bars are 10 nm.

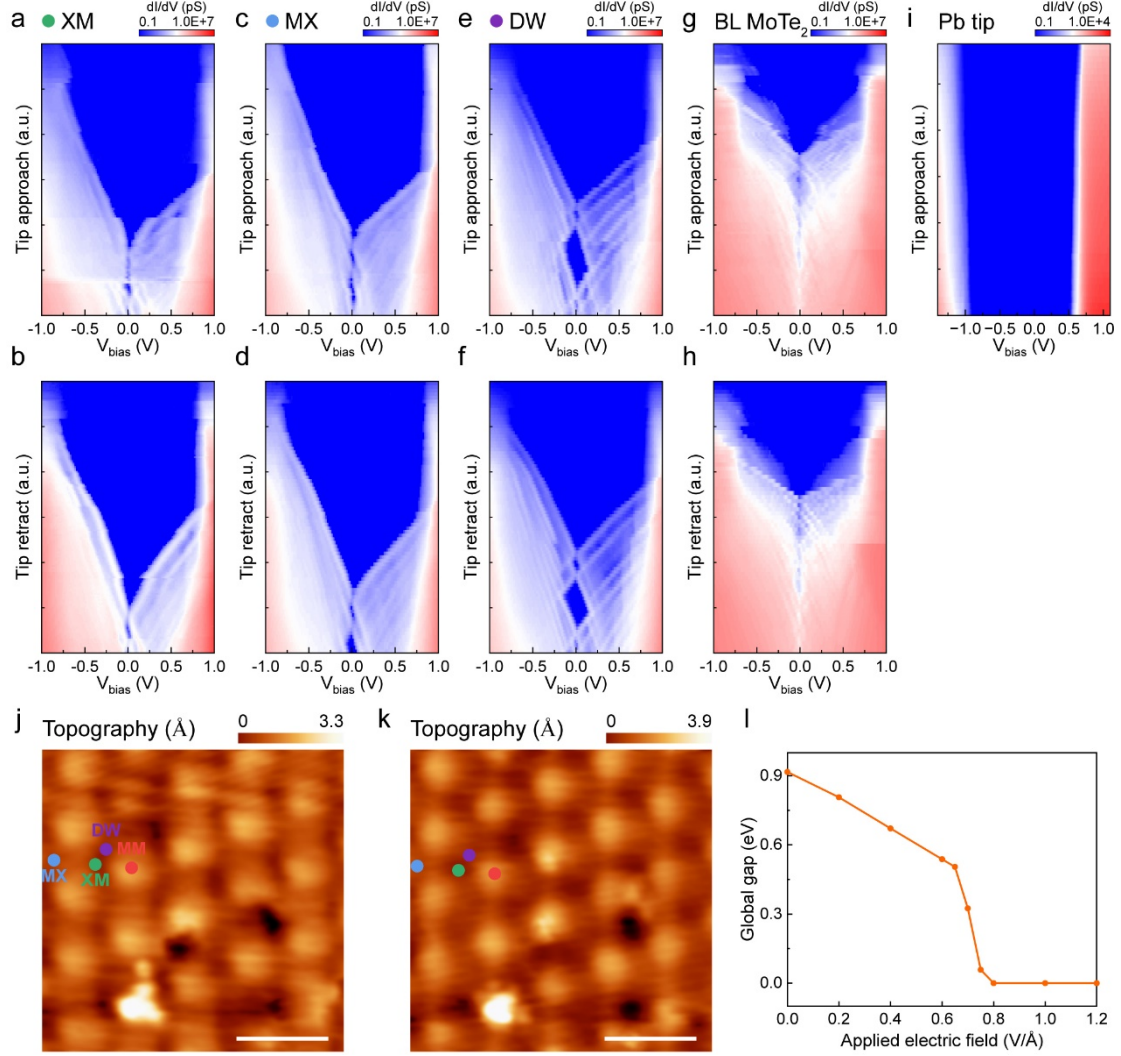


**Extended Data Fig. 4. Electronic structure of Bilayer MoTe<sub>2</sub>.** **a**, Schematic of the AB-stacked natural bilayer MoTe<sub>2</sub>. **b-c**, DFT calculated band structure (**b**) and DOS spectrum (**c**) of bilayer MoTe<sub>2</sub>. **d-e**, STS  $dI/dV$  spectra taken at different tip-sample separations with large energy scale (**d**) and zoomed-in energy scale (**e**). Bias Modulation: 20 mV. **f**, Extracted out-of-plane decay constant of states at different energies. The states at energy near -0.7 V decay very fast outside the MoTe<sub>2</sub> plane, indicating they originate from K-valley bands.



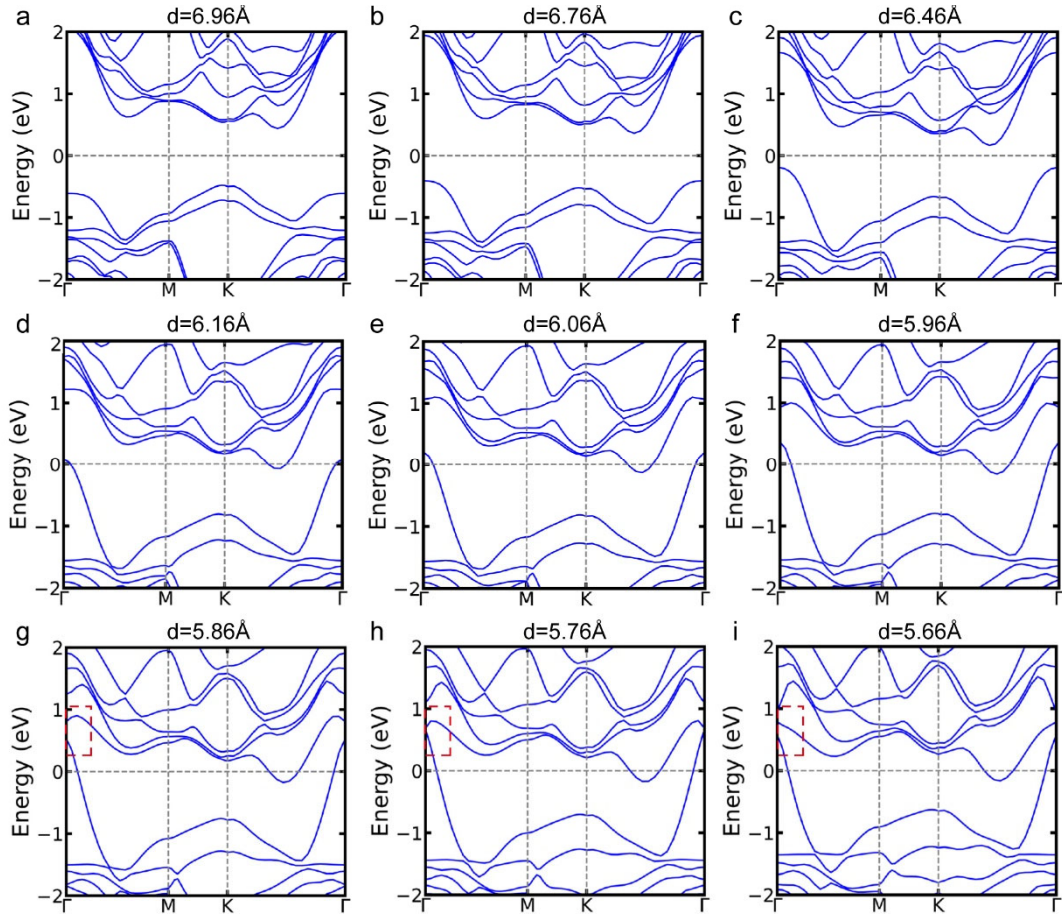
**Extended Data Fig. 5. DFT calculated band structures and DOS spectra of tMoTe<sub>2</sub>.**

**a**, DFT calculated band structures of tMoTe<sub>2</sub> with varied twist angles using a large-scale basis. **(b)** Corresponding DFT calculated DOS spectra.

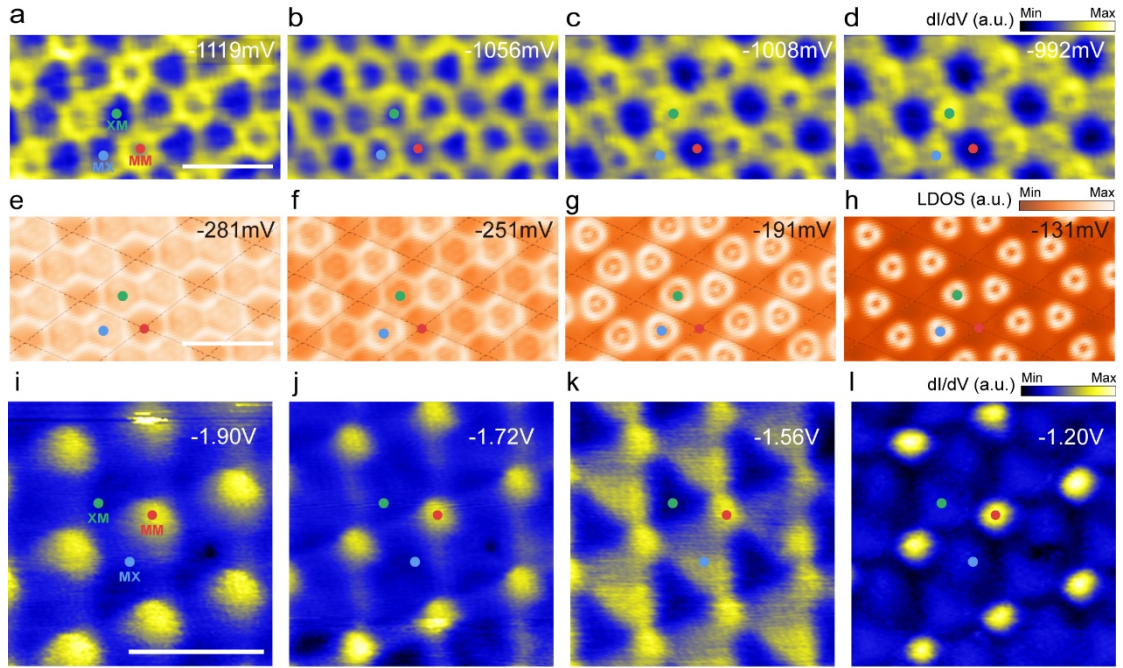


**Extended Data Fig. 6. Contact-STM measurements of tMoTe<sub>2</sub> (device B) and bilayer MoTe<sub>2</sub>.** **a-b**, STS  $dI/dV$  spectra plot taken on XM site with  $y$  axis indicating the pressure. We first record  $dI/dV$  spectra during the tip-approach process (**a**) and we measured  $dI/dV$  spectra again during the subsequent tip-retract process (**b**). Bias Modulation: 20 mV. **c-d**, STS  $dI/dV$  spectra plot taken on MX site recorded during the tip-approach process (**c**) and during the tip-retract process (**d**). Bias Modulation: 20 mV. **e-f**, STS  $dI/dV$  spectra plot taken on DW site. Bias Modulation: 20 mV. **g-h**, STS  $dI/dV$  spectra plot taken on bilayer MoTe<sub>2</sub>. Bias Modulation: 10 mV. **i**, STS  $dI/dV$  spectra plot taken on bilayer MoTe<sub>2</sub> recorded during the tip-approach process using a soft Pb tip. Bias Modulation: 10 mV. **j-k**, STM topography of a tMoTe<sub>2</sub> region with  $\theta \approx 2.8^\circ$  (device B,  $V_{\text{bias}} = -1.65$  V and  $I = 50$  pA) taken before (**j**) and after (**k**) contact-STM measurements. High symmetry stackings are marked by dots. Scale bars are 10 nm. **l**, DFT calculated band gap suppression as a function of applied electric field. The spectra plots of (**a-h**) are recorded using a hard tungsten tip.

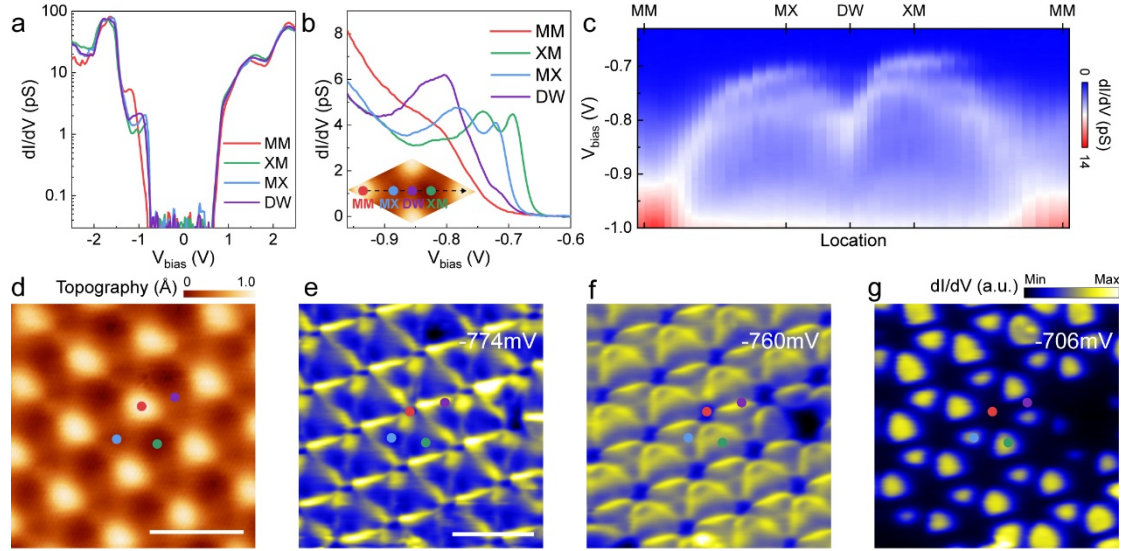




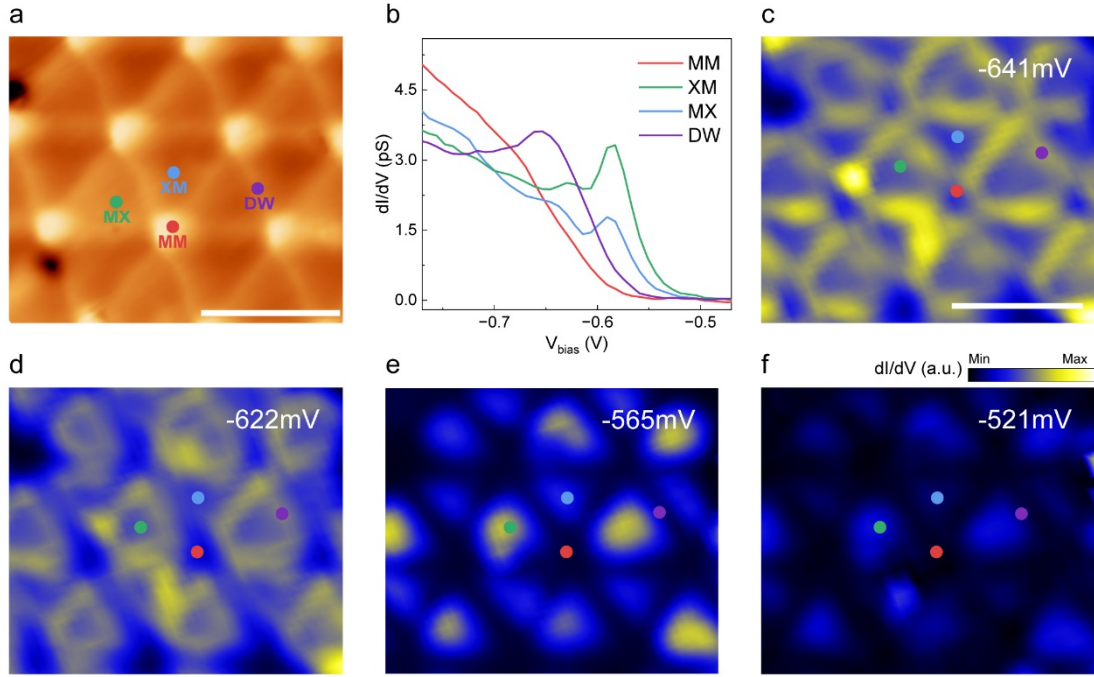
**Extended Data Fig. 7. DFT calculated band structures of tMoTe<sub>2</sub> with different inter-layer distances.** The red dashed rectangles in (g-i) indicate the evolution of band inversion at the  $\Gamma$ -valley with reduced inter-layer distance, giving to non-trivial topological characters.



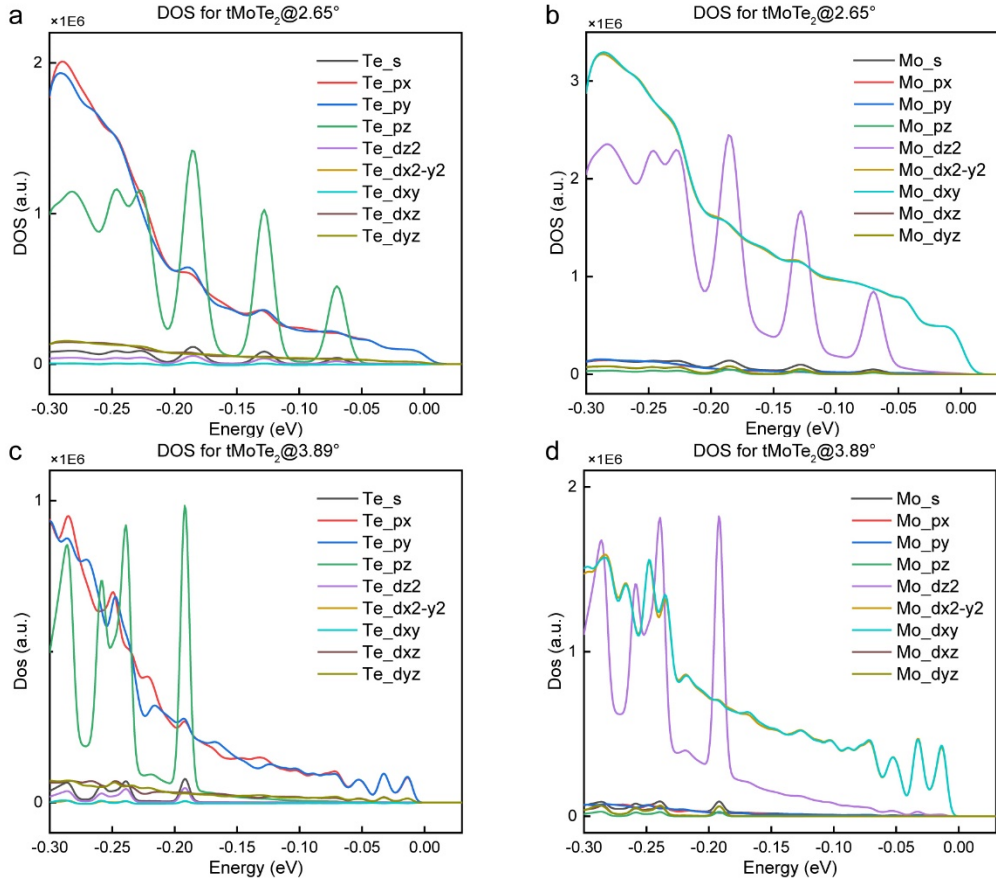
**Extended Data Fig. 8. More STS  $dI/dV$  maps and calculated LDOS distribution maps of  $t\text{MoTe}_2$ .** **a-d**, STS  $dI/dV$  maps taken on the same region as the main Fig. 4. Bias Modulation: 20 mV. **e-h**, DFT calculated LDOS distribution maps of the deep moiré flat bands from both  $\Gamma$  and K valley of  $t\text{MoTe}_2$ . **i-l**, Constant current STS  $dI/dV$  maps taken at higher biases showing the LDOS mainly located at MM regions. ( $I = 100$  pA, Bias Modulation: 50 mV) The scale bar is 10 nm.



**Extended Data Fig. 9. STS measurements of the moiré flat bands from both  $\Gamma$  and  $K$  valley of  $2.73^\circ$   $t\text{MoTe}_2$ .** **a-b**,  $dI/dV$  spectra taken at high-symmetry points on  $t\text{MoTe}_2$  (Device A,  $2.73^\circ$  region, strain 0.23%). The inset shows the STM topography at the same region with high symmetry stackings marked by colored dots. **c**, 2D plot of line  $dI/dV$  spectra taken along the dashed line in the inset of **(a)**. **d**, STM topography of a  $t\text{MoTe}_2$  region with  $\theta \approx 2.7^\circ$  (device A,  $V_{\text{bias}} = -2$  V and  $I = 30$  pA). **e-g**, STS mappings taken at different  $V_{\text{bias}}$ . The scale bar is 10 nm. Bias Modulation: 10 mV for **(a)**, 5mV for **(b-c)**, and 10mV for **(e-g)**.



**Extended Data Fig. 10. STS measurements of the moiré flat bands from both  $\Gamma$  and K valley of  $2.3^\circ$  tMoTe<sub>2</sub>.** **a**, STM topography of a tMoTe<sub>2</sub> region with  $\theta \approx 2.3^\circ$  (device A, strain 0.3%,  $V_{\text{bias}} = -1.7$  V and  $I = 30$  pA). **b**,  $dI/dV$  spectra taken at high-symmetry points on tMoTe<sub>2</sub>. **c-f**, Constant-height STS mappings taken at different  $V_{\text{bias}}$ . The scale bar is 10 nm. Bias Modulation: 20 mV.



**Extended Data Fig. 11. DFT calculated orbital contributions of  $\Gamma$  and K bands of tMoTe<sub>2</sub> with a twist angle of 2.65° and 3.89°.**  $\Gamma$ -valley bands originate from the  $d_{z^2}$  orbitals of Mo and Te, which possess out-of-plane momentum and therefore decay slowly outside the MoTe<sub>2</sub> layer. The K-valley states originate from the in-plane  $d_{xy}$  orbitals of Mo and the  $p_x$  and  $p_y$  orbitals of Te. These wavefunctions have large in-plane momentum and decay rapidly outside the MoTe<sub>2</sub> layer.